American Mineralogist, Volume 76, pages 1205–1217, 1991

On oriented titanite and rutile inclusions in sagenitic biotite

Yen-Hong Shau
Department of Geological Sciences, University of Michigan, Ann Arbor, Michigan 48109, U.S.A.
Houng-Yi Yang
Department of Earth Sciences, National Cheng Kung University, Tainan, Taiwan 70101, Republic of China
Donald R. Peacor
Department of Geological Sciences, University of Michigan, Ann Arbor, Michigan 48109, U.S.A.

Abstract

Well-oriented, needlelike inclusions occurring in sagenitic biotite in an orthogneiss from the Tananao complex, northeast Taiwan, have been studied by optical microscopy, transmission and analytical electron microscopy, and electron microprobe analysis. Titanite needles in three orientations combine to form equilateral triangles, and rutile needles in three other orientations generally intersect to form asterisk-shaped units. Titanite needles are elongated parallel to ⟨011⟩. They are oriented within {001} of biotite, and one of the three sets, which intersect at angles of 60°, is parallel to **a** of biotite. The $\{11\bar{1}\}$ or $\{43\bar{3}\}$ planes of titanite are approximately parallel to {001} of biotite. Rutile needles are elongated parallel to **c**, and rutile {100} is parallel to {001} of biotite. Of the three sets of rutile needles intersecting at angles of 60°, one is parallel to **b** of biotite. The preferred orientation of rutile inclusions in biotite is in accord with their mutually parallel planes of closest-packed anions and chains of edge-sharing octahedra. Titanite inclusions contain approximately 0.10 (Al + Fe) per formula unit, have space group *A2/a*, and give electron diffraction patterns that display streaking along **b*** and **c***. Rutile inclusions contain 0.2–0.3 wt% Fe_2O_3 (total Fe as Fe_2O_3), exhibit streaking and splitting of reflections in electron diffraction patterns, and display a planar microstructure parallel to {100}, which appears to consist of precipitated platelets that have the hematite structure and a probable composition $(Fe,Ti)_2O_3$. The titanite and rutile inclusions are inferred to have topotaxially precipitated through reactions occurring during retrogressive metamorphism when excess Ti and Ca were derived from biotite of igneous origin.

Introduction

The term "sagenitic texture" refers to the occurrence of slender, needlelike inclusions intersecting at angles of 60° and included in phlogopite, quartz, or other minerals (e.g., Gary et al., 1972). Although such acicular inclusions have long been thought to consist of rutile, titanite, hematite, tourmaline, zircon, apatite, or allanite (Moorhouse, 1959; Winchell, 1961; Rimšaite, 1964; Rimšaite and Lachance, 1966; Niggli, 1965; Gary et al., 1972; Deer et al., 1982), they have not been completely characterized. The most extensive study of sagenitic texture was carried out by Niggli (1965), who used electron microprobe techniques to analyze sagenites in biotite from plutonic rocks and gneisses and concluded that most of them consist of titanite but that some were rutile. Some well-oriented inclusions in the cores of phlogopite grains from a marble were identified optically as rutile (Rimšaite and Lachance, 1966). Titanite or rutile inclusions have been observed in biotite or phlogopite (Rimšaite, 1964; Rimšaite and Lachance, 1966; Niggli, 1965) and in chlorite produced by hydrothermal alteration of biotite (Rimšaite, 1964; Ferry, 1979; Parry and Downey, 1982; Veblen and Ferry, 1983; Eggleton and Banfield, 1985).

Sagenitic biotite occurs in the gneisses of the Tananao metamorphic complex on the island of Taiwan. This complex consists of pre-Tertiary pelitic schists, marbles, gneisses, metabasites, amphibolites, and serpentinites and crops out extensively along the eastern slope of the north-trending Central Mountain Range. Lo and Wang Lee (1981) performed X-ray analyses of the inclusions extracted from the sagenitic biotite and reported that they were titanite and sillimanite. To characterize these inclusions better and to establish their structural and crystallographic relations with the host biotite, samples of sagenitic biotite were collected from a pre-Tertiary orthogneiss near the village of Pihou, northeast Taiwan, and studied by optical microscopy, transmission and analytical electron microscopy (TEM and AEM), and electron microprobe analysis (EMPA).

Observation by optical microscopy

The orthogneiss of the present investigation is generally medium to coarse grained and has a granitoid texture. It

0003–004X/91/0708–1205$02.00

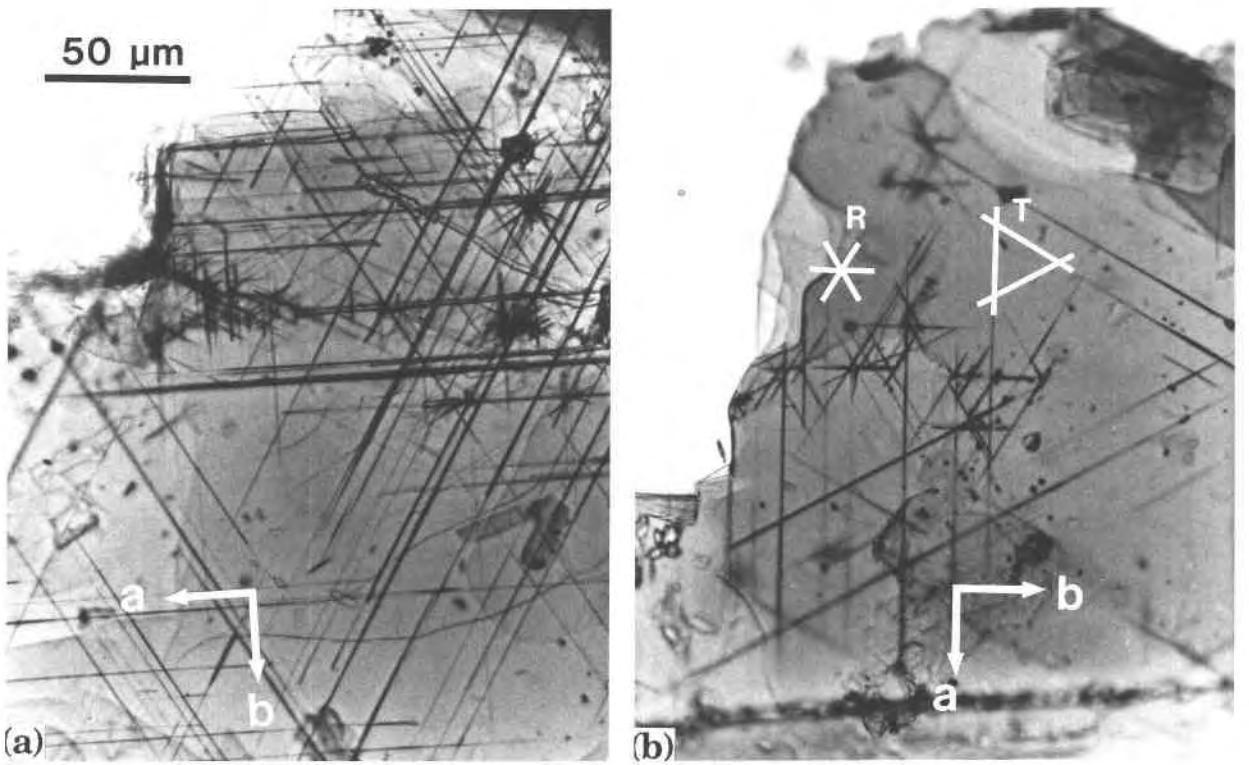

Fig. 1. (**a**) and (**b**) Photomicrographs of two sagenitic biotite flakes. Titanite (T) needles form equilateral triangles and rutile (R) needles form asterisks in the biotite host. One of the equilateral triangles and one of the asterisks are indicated by white solid lines. The **a** and **b** axes of biotite were chosen arbitrarily using one of the three directions of titanite and one of the three directions of rutile prisms, respectively. Plane-polarized light.

is composed of sodic plagioclase (An_{20-45}), quartz, biotite, and minor amounts of muscovite, potash feldspar, apatite, titanite (intergranular), garnet, chlorite, ilmenite, and trace amounts of calcite, which generally occurs as small inclusions (1–20 μm in diameter) lying along the parting planes or cleavages of plagioclase. The biotite commonly exhibits well-developed sagenitic texture. Some biotite grains are overgrown by chlorite or have layers intercalated with chlorite. No sagenitic inclusions have been observed in chlorite. However, a few isolated anhedral titanite inclusions up to 10 μm wide and 40 μm long have been observed in chlorite, with their long dimensions subparallel to {001} of chlorite. Subhedral titanite grains up to 1 mm long also occur at the intergranular sites among other major phases.

The sagenitic texture can best be examined in {001} sections of biotite. Very thin {001} sheets can easily be peeled from a biotite crystal, and the following characteristic features of sagenitic texture can be readily observed in immersion oil with a polarizing microscope (Fig. 1). Needlelike inclusions 0.1–2 μm (most are <0.5 μm) in width with high relief generally form oriented patterns consisting of equilateral triangles and asterisk-shaped units. Triangles are formed by three sets of parallel needles extending in three directions and intersecting at angles of 60° (±0.5°). An asterisk-shaped pattern is formed by three needles intersecting at angles of 60° but with a common origin. The needles forming asterisks are in general shorter than those forming equilateral triangles. However, the needles radiating from nearby asterisks may also intersect to form smaller triangles. When the equilateral triangle and asterisk patterns occur together in a single biotite flake, each of the three needles forming asterisks is oriented perpendicular to one of the three sets of needles forming equilateral triangles. The distribution of equilateral triangles is generally quite even throughout an entire flake of biotite, but the asterisks are clustered and distributed unevenly. Inclusions of other types and shapes, such as lath-shaped ilmenite and prismatic apatite crystals that are usually much larger than the needlelike inclusions, were also observed in some biotite grains. Edges of ilmenite grains appear to be partially replaced by anhedral titanite.

Equilateral triangles

Optical studies of single flakes of biotite have revealed that the abundant needlelike inclusions forming equilateral triangles are oriented parallel to {001} of biotite. One set of such needles is parallel to the **a** axis of biotite (Fig. 1). As it is difficult to distinguish the directions of **a** from **b** for the monoclinic cell of biotite (because of the small optic angle, $2V < 10°$) when biotite is observed in an

TABLE 1. AEM analyses of rutile and titanite inclusions in biotite and biotite from the Tananao orthogneiss, northeast Taiwan

Oxides (wt%)	Rutile		Titanite (ten analyses)		Biotite (eight analyses)	
	1E-RU2	1E-RU7	Range	Ave.	Range	Ave.
SiO_2	0.88	1.32	29.57–31.63	30.53	33.96–36.11	35.30
Al_2O_3	0.00	0.00	1.54–2.75	2.04	15.68–18.05	17.16
TiO_2	98.92	98.40	37.44–39.04	38.48	1.49–3.11	2.24
Fe_2O_3*	0.20	0.28	0.50–1.69	0.96	0.00	0.00
FeO*	0.00	0.00	0.00	0.00	20.50–23.73	21.71
MnO	0.00	0.00	0.00	0.00	0.17–0.26	0.21
MgO	0.00	0.00	0.00	0.00	8.21–9.42	9.01
CaO	0.00	0.00	25.35–28.56	26.54	0.00–0.10	<0.02
K_2O	0.00	0.00	0.37–0.53	0.45	8.88–10.05	9.37
Total**	100.00	100.00		99.00		95.00
Normalization factors: 2 O (rutile), 1 Si (titanite), and 22 O (biotite)						
Si	0.01	0.02	1.00	1.00	5.36–5.59	5.47
$^{[4]}$Al	0.00	0.00	0.00	0.00	2.64–2.41	2.53
$^{[6]}$Al	0.00	0.00	0.06–0.11	0.08	0.31–0.75	0.60
Ti	0.99	0.98	0.92–0.97	0.95	0.19–0.37	0.26
Fe^{3+}	<0.01	<0.01	0.01–0.04	0.02	0.00	0.00
Fe^{2+}	0.00	0.00	0.00	0.00	2.63–3.13	2.81
Mn	0.00	0.00	0.00	0.00	0.02–0.03	0.03
Mg	0.00	0.00	0.00	0.00	1.93–2.17	2.08
Ca	0.00	0.00	0.86–1.02	0.93	0.00–0.02	<0.01
K	0.00	0.00	0.02–0.02	0.02	1.75–2.02	1.85
Total	1.00	1.00		3.00		15.63

Note: Values of 2σ (from counting statistics) for cations of rutile: Si = 0.004, Ti = 0.01; for cations of titanite: Si = 0.02, Al = 0.008, Ti = 0.02, Fe = 0.002, Ca = 0.02, K = 0.005; for cations of biotite: Si = 0.08, Σ Al = 0.08, Ti = 0.02, Fe = 0.04, Mn = 0.01, Mg = 0.08, K = 0.04.

* Total Fe as Fe_2O_3 for rutile and titanite, and as FeO for biotite.

** Oxide weight percents normalized to total 100.00% for rutile, 99.00% for titanite, and 95.00% for biotite.

ordinary optical microscope, X-ray precession photographs were obtained to determine the orientations of **a** and **b** in the same biotite flakes as used in optical studies, however, reflections from the well-oriented inclusions were not visible in precession photographs, probably because of their very small volume. Optical observations at high magnification show that most of the needles do not really intersect but merely pass over or below others at different levels. The needles forming equilateral triangles exhibit inclined extinction, with an acute angle between the fast ray and the elongated axis (length fast). For needles belonging to any one of the three sets, some become extinct simultaneously with 18–25° clockwise rotation from the direction of polarization and the others with 18–25° counterclockwise rotation.

Asterisks

The needles forming asterisk-shaped patterns are also oriented parallel to {001} of biotite. Sets of three needles intersect with their ends meeting at a common central point. Clustering and overlapping of several asterisks were commonly observed (Fig. 1a). One of the three sets is parallel to the **b** axis of biotite. Each direction of the needles forming asterisks is therefore normal to the three directions, respectively, of the needles forming equilateral triangles. In contrast to the needles forming equilateral triangles, those forming asterisks exhibit parallel extinction and are length slow.

Observation and analysis by TEM and AEM

The biotite grains prepared for TEM observation were oriented in two directions. For electron beam orientations approximately parallel to **c** of biotite, very thin {001} sheets were glued onto 3-mm diameter Cu or Al washers (or slot-shaped grids) with epoxy resin. For beam orientations parallel to {001}, biotite grains having {001} nearly perpendicular to thin section surfaces were attached to the washers. The 3-mm diameter specimens were ion milled and then coated with a carbon film for observation with JEOL JEM-200CX, Hitachi H700-H, and Philips CM-12 scanning transmission electron microscopes (STEMs). Conventional TEM bright field and dark field images, selected area electron diffraction (SAED) patterns, and AEM analyses using the CM-12 STEM equipped with a Kevex energy dispersive spectrometer (EDS, Quantum detector) were obtained. AEM analyses were obtained at counting rates of 200–400 cps with acquisition times of 200 s (live time) and from thin edges of ion-milled specimens where absorption effects were negligible. The needlelike inclusions of titanite and rutile are usually less than 0.5 μm in width, and although unresolved by EMPA, they can be precisely analyzed by AEM with a probe ~0.01 μm in diameter (Table 1). The host biotite was also analyzed by AEM (with a rastering area of 0.2 μm × 0.2 μm) for comparison with EMPA results (Table 2). Standard deviations calculated from counting statistics for major elements are similar for both EMPA and AEM analyses. The thin foil approximation as proposed by Cliff and Lorimer (1975) was used to calculate element proportions using experimentally determined k-factors. As only the relative concentrations of elements can be determined by these k-factors, weight percents of the oxides for a mineral were calculated by normalization, based on anhydrous totals that were as-

Table 2. Electron microprobe analyses of biotite, muscovite, chlorite, and titanite from Tananao orthogneiss, northeast Taiwan

Oxides and elements (wt%)	Biotite (27 analyses)		Muscovite	Chlorite	Titanite*	
	Range	Ave.	Mu19	C101	I	R
SiO_2	35.03–35.56	35.35	46.62	24.75	30.69	30.56
Al_2O_3	16.13–17.14	16.47	32.98	20.68	2.26	1.00
TiO_2	1.71–3.83	2.90	0.87	0.04	36.39	38.20
Cr_2O_3	0.00–0.04	0.01	0.03	0.01	0.00	0.00
$FeO(Fe_2O_3)$**	20.80–22.57	21.98	2.12	28.14	0.54	0.43
MnO	0.20–0.36	0.29	0.04	0.48	0.21	0.05
MgO	7.65–8.64	8.20	1.42	13.03	0.00	0.00
CaO	0.00–0.10	0.03	0.03	0.06	28.77	28.48
BaO	0.06–0.32	0.17	0.28	0.08	0.14	0.02
Na_2O	0.05–0.12	0.08	0.49	0.04	0.03	0.00
K_2O	9.33–9.65	9.51	10.40	<0.01	0.02	0.01
F	0.03–0.30	0.14	0.00	0.09	0.57	0.25
Cl	0.00–0.05	0.02	0.02	0.02	0.00	0.02
Total		95.15	95.30	87.42	99.62	99.02
Normalization factors: 22 O (B and M), 28 O (C), and 1 Si (T)						
Si	5.479–5.545	5.505	6.251	5.346	1.000	1.000
$^{[4]}Al$	2.521–2.455	2.495	1.749	2.654	0.000	0.000
$^{[6]}Al$	0.431–0.694	0.528	3.464	2.610	0.087	0.039
Ti	0.208–0.446	0.339	0.088	0.007	0.892	0.940
Cr	0.000–0.005	0.001	0.003	0.002	0.000	0.000
$Fe^{2+}(Fe^{3+})$**	2.712–2.936	2.862	0.238	5.083	0.013	0.011
Mn	0.026–0.047	0.038	0.005	0.088	0.006	0.001
Mg	1.771–2.016	1.904	0.283	4.196	0.000	0.000
$^{[6]}\Sigma$		5.672	4.081	11.986	0.998	0.991
Ca	0.000–0.017	0.005	0.004	0.014	1.004	0.999
Ba	0.004–0.020	0.010	0.015	0.007	0.002	<0.001
Na	0.015–0.036	0.023	0.128	0.016	0.002	0.000
K	1.851–1.927	1.888	1.779	0.002	0.001	<0.001
Σ cations		15.598	14.007	20.025	3.007	2.990
F	0.015–0.145	0.067	0.000	0.061	0.059	0.025
Cl	0.000–0.012	0.005	0.005	0.006	0.000	0.001

Note: Values of 2σ (from counting statistics) for cations of biotite: Si = 0.077, Σ Al = 0.042, Ti = 0.014, Cr = 0.0003, Fe = 0.092, Mn = 0.007, Mg = 0.038, Ca = 0.0008, Ba = 0.001, Na = 0.004, K = 0.045, F = 0.027, Cl = 0.002.

* I = intergranular, R = replacing ilmenite inclusions in biotite.

** Total Fe as FeO for biotite, muscovite, and chlorite, and as Fe_2O_3 for titanite.

sumed to be 95.0% for biotite, 99.0% for titanite, and 100.0% for rutile (e.g., Shau et al., 1991). Hole-count spectra amount to only 0.5% of the total counts for biotite spectra (~60000 counts for each analysis) acquired from thin edges. Nevertheless, such stray radiation contributes up to 30% of intensities for elements considered minor in titanite and rutile (e.g., K and Fe of titanite). Therefore, analytical data for titanite and rutile were corrected by subtracting hole-count spectra. For biotite, the contribution of the hole-count spectrum was negligible.

Rutile

Major Ti and O and minor Si and Fe were detected with AEM analyses of needles forming the asterisks (Table 1). The electron diffraction patterns from these three sets of needles were indexed using the cell parameters of rutile ($a = 4.59$, $c = 2.96$ Å). These data, in combination with the optical properties (very high relief, parallel extinction, and length slow), show that those needles consist of rutile.

Figure 2 shows SAED patterns and a TEM bright field image obtained from a rutile inclusion within a biotite flake that was oriented with (001) perpendicular to the electron beam. The electron beam direction was thus approximately parallel to **c*** of biotite. It was also parallel to **a** (arbitrarily defined as [010]) of rutile. The SAED pattern in Figure 2a therefore includes the rutile [010] zone pattern and a slightly misoriented biotite [001] zone pattern. The [001] SAED pattern of biotite is a hexagonal net that includes **a*** and **b***. The [010] SAED pattern of rutile exhibits *h*0*l* reflections showing elongation or streaking along **a*** (Fig. 2a). The axes **c*** and **a*** of rutile are each exactly parallel to **b*** and **a*** of biotite, respectively, when projected onto the plane of the photograph. The [001] axis of biotite is slightly tilted toward $-\mathbf{a}^*$, as is evident from the asymmetric intensity distribution of biotite reflections. The **a** axis (instead of **a***) of biotite is actually nearly parallel ($\pm 2°$) to the plane of the photograph when the tilt angle and β angle of biotite are considered. Therefore, it is inferred that **c*** of rutile is parallel to **b*** of biotite whereas **a*** ([100]*) of rutile is parallel to **a** of biotite; i.e., $\mathbf{c}_R \| \mathbf{b}_B$ and $(010)_R \| (001)_B$.

A [010] SAED pattern from another rutile inclusion shows the following features: an additional set of reflections occurring as split reflections along **a***, slight streaking of reflections along **a***, and superstructurelike reflections that triple the spacing $d_{(101)}$ along [101]* or [10$\bar{1}$]* (Fig. 3a). The additional set of reflections displays a perfect hexagonal-net pattern as for biotite. However, the smallest vectors containing the extra reflections along **a***

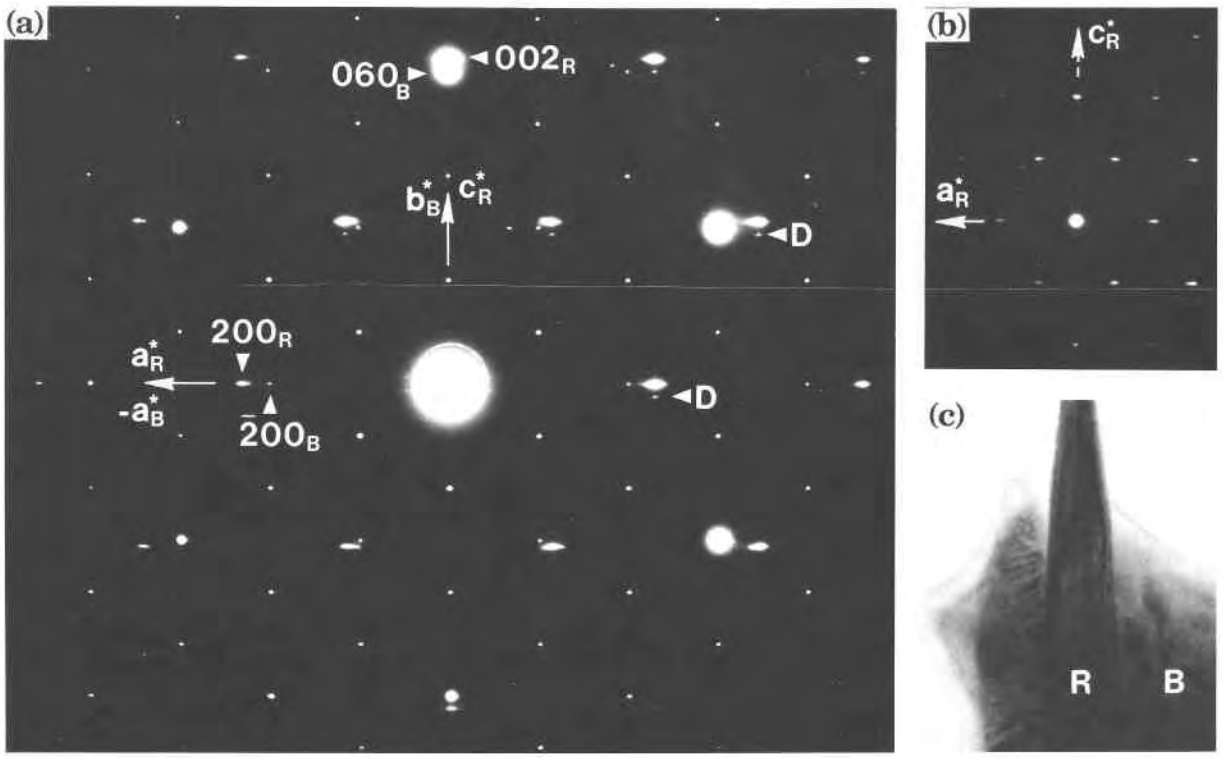

Fig. 2. (**a**) SAED pattern of the [001] zone of biotite (B) (slightly misoriented) and of the [010] zone of a rutile needle (R). The **b*** axis of biotite coincides with **c*** of rutile, whereas the projection of **a*** of biotite coincides with **a*** of rutile. Diffuse reflections of rutile are elongated parallel to **a***. The reflections labeled D are caused by double diffraction (cf. Hirsch et al., 1977). (**b**) SAED pattern with a smaller camera length showing reflections only from the rutile needle. The reflections caused by double diffraction are not present since there are no reflections from biotite. (**c**) TEM bright field image of the rutile needle elongated parallel to its **c** axis and to **b** of biotite. The maximum width of the needle is 0.15 μm.

of rutile correspond to a d-value of 2.52 ± 0.04 Å (calibrated from rutile cell parameters), which can be indexed as the 110 reflection of hematite (a = 5.034 Å and $d_{(110)}$ = 2.517 Å for the hexagonal cell) or ilmenite (a = 5.088 Å and $d_{(110)}$ = 2.544 Å) within measurement error. These reflections are thus identified as the [001] zone pattern of hematite-ilmenite with (001) parallel to (010) of rutile. A dark field image that was formed by using the adjacent $\bar{2}00_R$ and 110_H reflections shows wavy stripes extending parallel to **c** (Fig. 3b).

The tetragonal symmetry of rutile implies that the platelets are also oriented with (001) parallel to (100) of rutile. The wavy stripes shown in Figure 3b thus correspond to such edge-on platelets and cause the streaking of reflections along **a*** of rutile. These edge-on platelets also contribute to a [110] zone pattern of hematite-ilmenite, which includes a 006 reflection ($d_{(006)}$ = 2.29 Å for hematite) superimposed on the $\bar{2}00$ reflection of rutile and therefore contributes to the white contrast of the wavy stripes in Figure 3b. The superstructurelike reflections along ⟨101⟩* can be derived from dynamic diffraction (or double diffraction, cf. Hirsch et al., 1977) of the [110] zone reflections of hematite-ilmenite and the [010] zone reflections of rutile. Similar platelet microstructures were observed in Fe-bearing rutile in metapelites from Vermont (Banfield and Veblen, 1991) and in synthetic nonstoichiometric rutile (e.g., Bursill et al., 1984).

Figure 4 shows three rutile needles intersecting at a triple junction, with an angle of 120° between each pair. As the prism axes of rutile needles were observed with an optical microscope to lie in the (001) plane of biotite, the collective TEM and optical data suggest that the rutile inclusions and biotite matrix have the following crystallographic relationship: for one of the three sets of rutile needles, **c** of rutile (the prism direction) is parallel to **b** of biotite, whereas $\mathbf{a}_1$ and $\mathbf{a}_2$ of rutile coincide with **a** and **c*** of biotite, respectively. In other words, (010) of rutile is parallel to (001) of biotite. The **c** axes of the other two sets of rutile needles are oriented 120° (or 60°) clockwise and counterclockwise from the **b** axis of biotite in (001) of biotite. Their (010) planes are also parallel to (001) of biotite. Although almost all rutile needles were oriented as described above, one exception has been observed in which (110) of rutile was parallel to (001) of biotite.

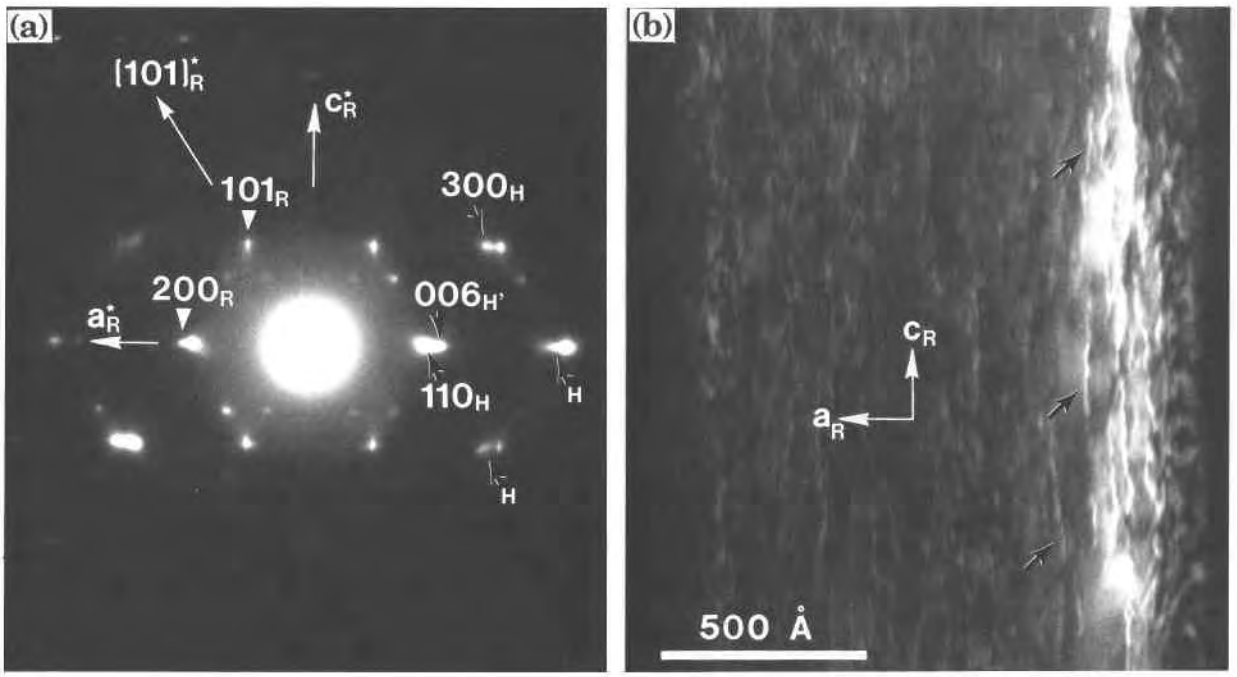

Fig. 3. (a) SAED pattern of the [010] zone of rutile. Reflections are diffuse and there are extra reflections (indicated by black arrows; see text) arranged parallel to **a***. The reflection $006_{H'}$ superimposes on the reflection 200_R. Superperiodic reflections tripling d_{101} lie along [101]* or [10$\bar{1}$]*. R = rutile, H = platelets$\|(010)_R$, H′ = platelets$\|(100)_R$. (b) A TEM dark field image formed from the reflections including $\bar{2}00_R$, $006_{H'}$, and 110_H. The wavy stripes (indicated by black arrows) extending along **c** are representative of the edge-on platelets parallel to $(100)_R$.

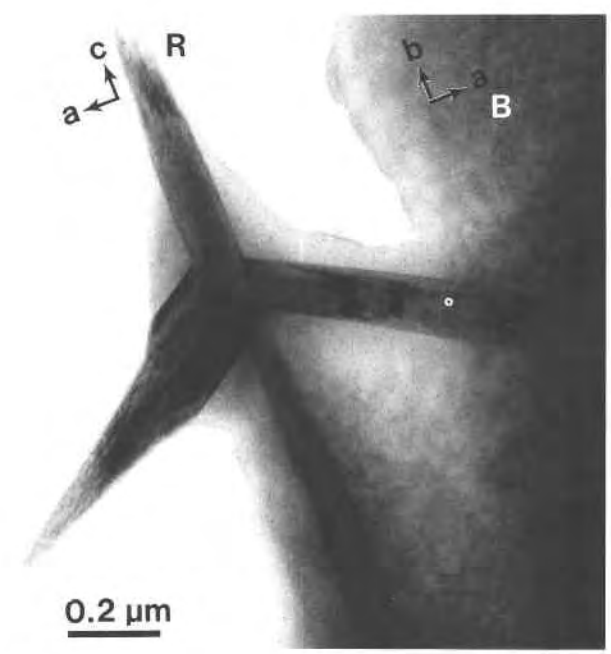

Fig. 4. TEM bright field image of three rutile (R) needles intersecting at a triple junction and partly embedded in biotite (B). A fourth needle is located at a level below the three intersecting needles.

Titanite

The electron diffraction patterns of the needlelike inclusions forming equilateral triangles can be indexed with the cell parameters of synthetic titanite (a = 7.07, b = 8.72, c = 6.57 Å, b = 113.86°, Speer and Gibbs, 1976) for space group $A2/a$. The AEM analyses for these needles reveal the presence of major Si, Ca, Ti, and O with minor Al, Fe, and K (Table 1). These data collectively show that the needlelike inclusions that are elongated parallel to **a** of biotite and oriented as equilateral triangles are titanite.

Figure 5 shows a TEM image and a SAED pattern with [101] of titanite and (001) of biotite parallel to the electron beam, for which the specific zone of biotite is not identified. The axis [11$\bar{1}$]* of titanite is parallel to **c*** of biotite, indicating that (11$\bar{1}$) of titanite is parallel or nearly parallel to (001) of biotite. A [213] SAED pattern (not shown here) of the same titanite inclusion also gave a diffraction pattern with [11$\bar{1}$]* of titanite parallel to **c*** of biotite and therefore confirmed that $(11\bar{1})_T\|(001)_B$ for that titanite crystal. Weak and diffuse streaks parallel to **b*** of titanite can be observed in the SAED pattern (Fig. 5a).

Figure 6 is a SAED pattern of titanite [11$\bar{1}$] and slightly misoriented biotite [001] zones. Comparison of the diffraction pattern with the corresponding image shows that the prismatic titanite crystal is elongated parallel to **a*** of

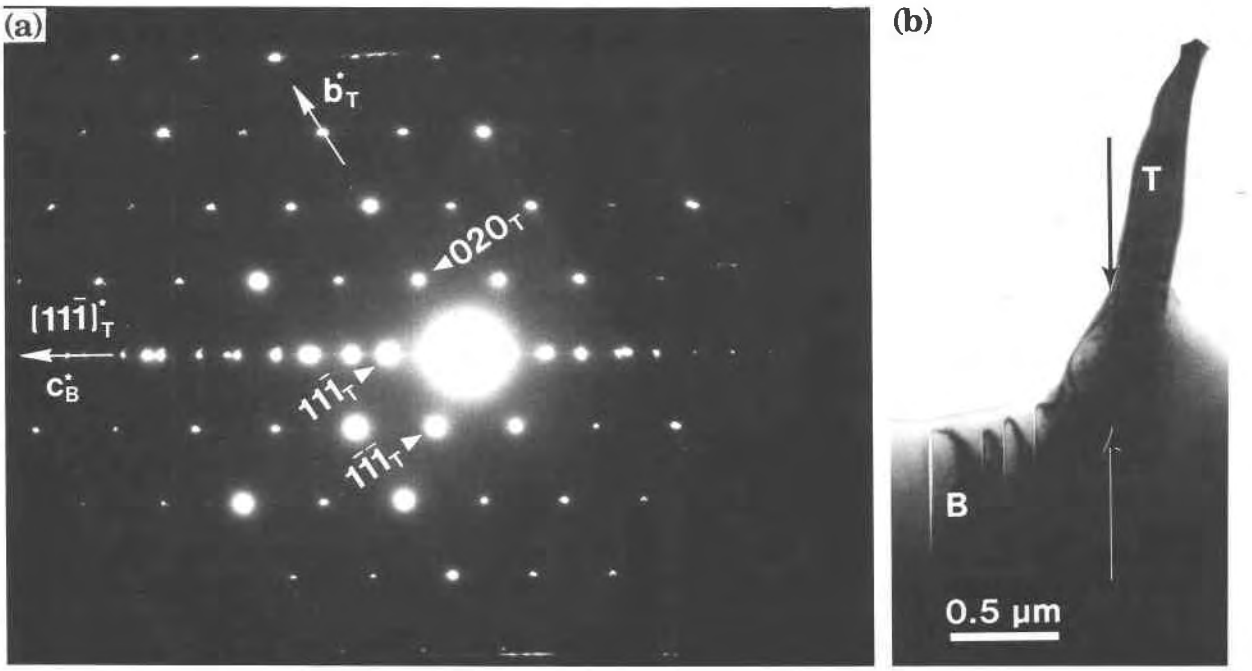

Fig. 5. (a) SAED pattern of the [101] zone of titanite (T) and of biotite (B) where **c*** of biotite is parallel to $[11\bar{1}]^*$ of titanite; i.e., $(11\bar{1})$ of titanite is parallel to (001) of biotite. There are weak and diffuse streaks parallel to **b*** of titanite. (b) Bright field image showing that the interface (indicated by arrows) between the titanite needle and biotite host is parallel to (001) of biotite.

biotite. However, the difference in intensity between biotite $h00$ and $\bar{h}00$ reflections suggests that the [001] axis was tilted toward $-\mathbf{a}^*$, and **a** is inferred to be the axis that is actually parallel to the prism axis of titanite when the tilt angle and β angle of biotite are taken into account. It is thus consistent with the optical observation that prism axes of titanite are parallel to (001) of biotite. The prism axis of titanite is perpendicular to $[2\bar{1}1]^*$; i.e., it is parallel to $(2\bar{1}1)$. Other diffraction patterns (not shown), consisting of the biotite [001] zone and (1) titanite $[21\bar{1}]$ zone and (2) titanite [411] zone, show that the prism axes of titanite are parallel to $(1\bar{1}1)$ and $(0\bar{1}1)$ of titanite, respectively, and are also parallel to **a** of biotite. Therefore, the prism axis of titanite was parallel to the zone axis of $(2\bar{1}1)$, $(1\bar{1}1)$, and $(0\bar{1}1)$, i.e., to [011] of titanite.

Orientations of planes and axes of titanite and biotite as determined by diffraction relations were plotted on a stereographic projection to characterize their relations. The results, based on the reflections in Figure 6, show that the prism axis and [011] of titanite, and **a** of biotite are parallel to each other (±0.5°) when projected on (001) of biotite. They also show that $(11\bar{1})$ of titanite is nearly parallel to (001) of biotite, with an interfacial angle of 2.2°. The direction of the slow and fast rays of titanite can be determined from the orientation of the crystallographic axes of titanite, and thus the extinction angle can be predicted. The extinction angle as predicted for the above relationship (Fig. 6) in which (001) of biotite is normal to the optical axis is 22 ± 2°. It is measured clockwise from the fast-ray direction to the prism axis of titanite. However, because the titanite prisms of any one parallel set can be elongated parallel to either [011] or $[0\bar{1}1]$ (symmetrically equivalent), both clockwise and counterclockwise extinction angles should be observed for any one set. The observation of such symmetrically related extinctions (see above) verifies the orientation relation and shows that it is the general relation for most needlelike titanite.

A SAED pattern corresponding to [011] of titanite and [100] of biotite, as obtained from a titanite needle parallel to the beam, shows that [011] of titanite is parallel to **a** of biotite (Fig. 7). However, (001) of biotite is parallel to $(43\bar{3})$ rather than $(11\bar{1})$ of titanite, and **c*** of biotite and $[11\bar{1}]^*$ of titanite are inclined by approximately 10°, in contrast to the above relation in Figures 5 and 6. A $[3\bar{1}3]$ SAED pattern of titanite (not shown), for which the beam was parallel to (001) of biotite, also indicates that $(43\bar{3})_T \| (001)_B$.

In other electron diffraction patterns, (001) of biotite was found to be parallel to nearly parallel to (001), $(10\bar{1})$, $(01\bar{1})$, or $(\bar{4}10)$ of titanite. Assuming that the prism axes of such titanite needles are also parallel to **a** of biotite, stereographic projections show that they must have extinction angles different from those usually observed (18–25°) for the titanite needles forming equilateral triangles. Titanite inclusions with such orientations are rare relative to those commonly occurring orientations with $(11\bar{1})_T$ or $(43\bar{3})_T \| (001)_B$ and $[011]_T \| [100]_B$.

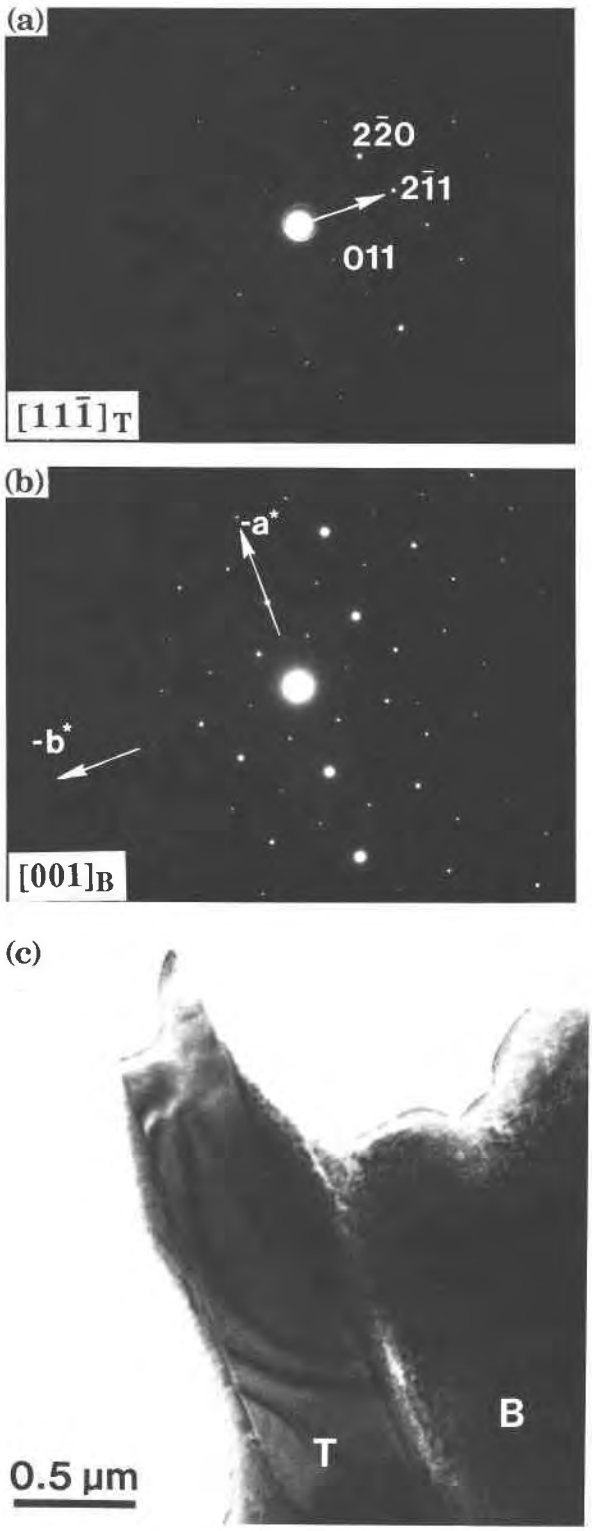

Fig. 6. (**a**) SAED pattern of the [11$\bar{1}$] zone of titanite. The arrow is parallel to [2$\bar{1}$1]*. (**b**) SAED pattern of the [001] zone of biotite ([001] was slightly tilted toward $-\mathbf{a}^*$). (**c**) The corresponding bright field image shows that the prism axis of titanite (T) is perpendicular to [2$\bar{1}$1]* of titanite and parallel to the projection of **a*** of biotite.

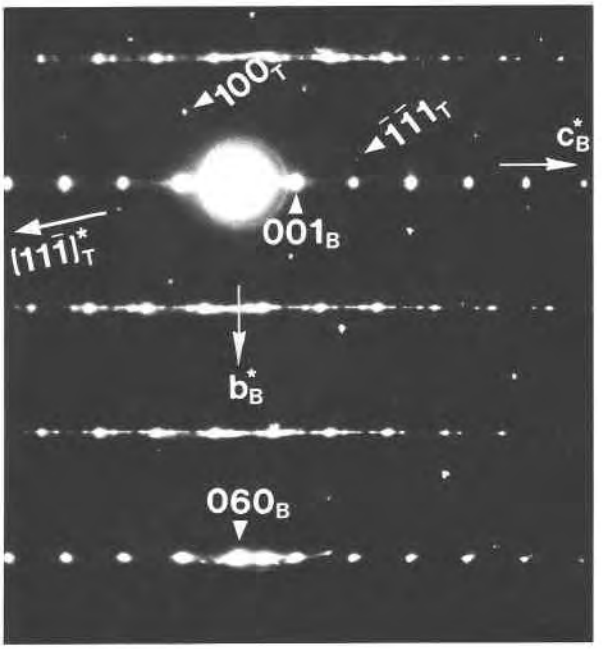

Fig. 7. SAED pattern of the [011] zone of titanite (T) and the [100] zone of biotite (B) obtained from a sample with the prism axis of titanite parallel to the electron beam. The axis [1$\bar{1}$1]* of this titanite needle is not parallel to **c*** of biotite.

Electron microprobe analyses (EMPA)

Compositions of biotite, muscovite, chlorite, intergranular titanite, and titanite replacing ilmenite inclusions in biotite were obtained with a Cameca Camebax electron microprobe using 12 kV accelerating voltage and 10 nA beam current (Table 2). The standards include diopside (Si,Ca), andalusite (Al), geikielite (Ti), uvarovite (Cr), ferrosilite (Fe), rhodonite (Mn), olivine (Mg), sanbornite (Ba), albite (Na), potassium feldspar (K), F-rich topaz (F), and barium chlorine apatite (Cl). The beam was rastered over an area 6 μm $\times$ 6 μm for both standards and specimens to reduce loss of alkali cations resulting from diffusion.

The composition of biotite obtained with EMPA is consistent with that obtained with AEM, except that values for minor elements are better defined with EMPA. The range and average values for 27 microprobe analyses of biotite and the resulting compositions are listed in Table 2. Biotite that has been overgrown or partially replaced by chlorite generally contains less TiO_2. Muscovite contains less TiO_2 and more Na_2O, whereas chlorite contains much less TiO_2 but more MnO than biotite.

Structural formulae of titanite were normalized to 1 Si, as consistent with occupancy of the tetrahedral site only by Si and assignment of all Ti, Fe^{3+}, and Al to the octahedral site (e.g., Higgins and Ribbe, 1976). The coarser grained titanite, which either replaces ilmenite inclusions (in biotite) or occurs at intergranular sites, gives rise to titanite structural formulae approaching ideal values (Ta-

ble 2). The titanite also contains 0.25–0.79 wt% of F. However, the titanite replacing ilmenite contains much less Al_2O_3 and F but slightly more TiO_2. When compared with the acicular titanite inclusions in biotite, the coarser-grained titanite exhibits lower Fe_2O_3 and K_2O contents and slightly higher CaO content.

Discussion

Mineral chemistry and microstructures of rutile and titanite

Optical microscopy, AEM microanalysis, and electron diffraction have shown that the needlelike inclusions forming the asterisks are rutile and those forming the equilateral triangles in projection on (001) of biotite are titanite. The optical observations and electron diffraction data show that the rutile and titanite inclusions generally, but not always, have a preferred orientation in biotite.

The rutile inclusions contain minor amounts of Si and Fe but no detectable Ta^{5+} or Nb^{5+} that may be coupled with substitution of Fe^{3+} or Fe^{2+}, as observed by others for rutile (cf. analyses compiled in Deer et al., 1962b, Rumble, 1976). As described above, the SAED patterns of rutile exhibit features of streaking, reflections from an extra phase, and superstructurelike reflections. The streaking of reflections along **a*** of rutile in SAED patterns (Figs. 2 and 3) implies the presence of platelet structures parallel to (100) of rutile, as directly seen in dark field images (Fig. 3b). The reflections from these platelets, though most are superimposed on the reflections of rutile, can be indexed as hematite-ilmenite with $(001)_H \| (100)_R$. The superstructurelike reflections can also be attributed to dynamic diffraction from these platelets and rutile. Furthermore, the additional set of reflections (Fig. 3a) is consistent with the [001] zone pattern of hematite-ilmenite that is oriented with $[\bar{1}20]_H \| \mathbf{c}_R$ (i.e., $\mathbf{a}_{3,H} \perp \mathbf{c}_R$) and $(001)_H \| (010)_R$.

Similar streaking and splitting of reflections, superstructurelike reflections, and platelet structures were observed by Banfield and Veblen (1991) in Fe-bearing rutile (FeO = 0.5–3 wt%) from chlorite- to staurolite-grade metapelites. They have concluded that coherently intergrown hematite (or ilmenite) platelets precipitated parallel to (100) and (010) of rutile and that the streaking of reflections is due to platelets of irregular spacing, whereas the superstructurelike reflections are caused by dynamic diffraction. Putnis and Wilson (1978) and Putnis (1978) noted that experimental annealing of natural Fe-bearing rutile (FeO = 0.55 wt%) at temperatures between 475 and 595 °C resulted in precipitation of two transitional phases (coherent Fe-rich precipitates) and hematite. Bursill et al. (1984) observed {100} platelet defects, often occurring in association with crystallographic shear planes, in synthetic nonstoichiometric rutile (TiO_{2-x}, $0 \le x \le 0.0035$). They suggested that the platelet defects precipitated as a Ti_2O_3 phase with the corundum-type structure and that the microstructures are strongly determined by cooling history. The {100} platelet defects that they observed have zigzag changes in orientation and are similar to the wavy stripes described above. Putnis (1978) and Bursill et al. (1984) proposed different structural models for the precipitated phases to interpret the superstructurelike reflections tripling d_{101} of rutile (see Banfield and Veblen, 1991 for review). Miser and Buseck (1988) observed polysynthetic twinning on {100} of rutile and other defect structures in O-deficient rutile that occur in mudstone xenoliths from an environment with low f_{O_2}. As evidenced by the SAED patterns and TEM images (Figs. 2 and 3), the rutile inclusions in the sagenitic biotite from the Tananao orthogneiss contain precipitated {100} platelets that have the hematite structure. However, these platelets are likely to have Ti substituting for Fe, as implied by the low contents of Fe_2O_3 (~0.2 wt%) in rutile and the abundance of platelets (Fig. 3b).

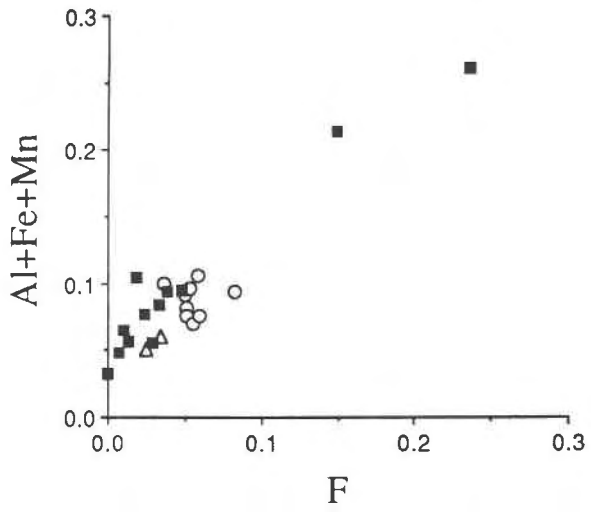

Fig. 8. Plot of Al + Fe + Mn vs. F in ion numbers per formula unit for titanite from the Tananao orthogneiss (open symbols), including intergranular titanite (circles) and titanite replacing ilmenite inclusions in biotite (triangles). The positive trend is more obvious when the analyses of titanite compiled by Higgins and Ribbe (1976) are also plotted (solid squares).

The titanite inclusions always contain minor amounts of Al, Fe, and K in addition to the major elements Si, Ti, and Ca, even after subtraction of hole counts (Table 1). The composition of titanite is generally affected by substitutions such as $(Al,Fe)^{3+} + (F,OH)^- = Ti^{4+} + O^{2-}$ (Higgins and Ribbe, 1976; Deer et al., 1982). Although F and OH could not be detected by AEM for the titanite inclusions, microprobe analyses of the coarser grained titanite indicated that F contents have a positive correlation with those of Al + Fe (Fig. 8).

The substitution of Al and Fe for Ti and of OH, Cl, and F for O in natural titanite favors the formation of domains between which the directions of Ti displacement in TiO_6-octahedra reverse from $+\mathbf{a}$ or $-\mathbf{a}$ (Speer and Gibbs, 1976; Taylor and Brown, 1976). Synthetic titanite undergoes a reversible, displacive phase transition at 220

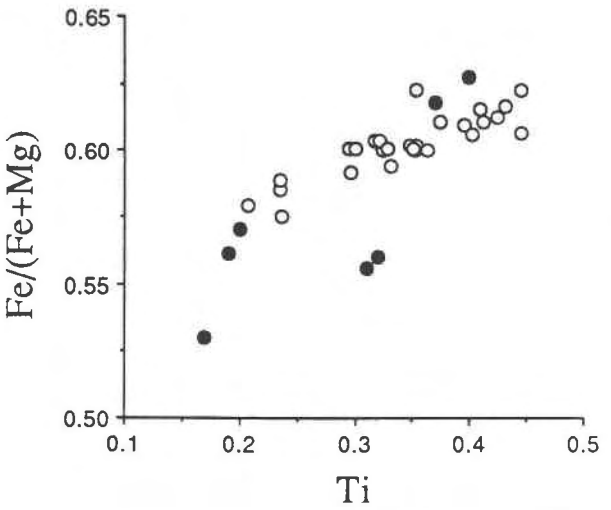

Fig. 9. Plot of Fe/(Fe + Mg) vs. Ti per formula unit (22 O) for sagenitic biotite from the Tananao orthogneiss. Analyses obtained with AEM (solid circles) and EMPA (open circles), respectively.

± 20 °C from space group $P2_1/a$ to $A2/a$ (Taylor and Brown, 1976). Higgins and Ribbe (1976) demonstrated with X-ray diffraction and electron diffraction data that the space group of natural titanite varies from $P2_1/a$ for relatively pure end-member compositions to $A2/a$ with increasing substitution of Al and Fe. The SAED patterns of titanite inclusions in the sagenitic biotite generally exhibit no reflections with $k + l$ odd, as consistent with space group $A2/a$, but some of them have faint diffuse streaks parallel to **b*** (Fig. 5a) or **c*** (not shown). The results further demonstrate that titanite with significant Al and Fe has disorder in Ti displacements as consistent with space group $A2/a$.

Chemical relations for titanian biotite

Biotite commonly has up to a few weight percent of TiO_2 (1–5 wt%) and less than 1 wt% of CaO (e.g., Foster, 1960a, 1960b; Deer et al., 1962a). The Ti in biotite is located in octahedrally coordinated sites, and its substitution is coupled with substitution of Al for Si (i.e., Ti-Tschermak's substitution: $Ti^{4+} + 2Al^{3+} = Mg^{2+} + 2Si^{4+}$; e.g., Robert, 1976; Guidotti, 1984; Hewitt and Wones, 1984), substitution of O for OH (e.g., Bohlen et al., 1980), or octahedral vacancies (e.g., Dymek, 1983 and references therein). Therefore, titanian biotite may consist of one or more of the components $K_2(Mg,Fe)_5TiSi_4Al_4O_{20}(OH)_4$, $K_2(Mg,Fe)_5TiSi_6Al_2O_{22}(OH)_2$, or $K_2(Mg,Fe)_4TiSi_6Al_2O_{20}(OH)_4$. The biotite in the Tananao orthogneiss contains 1.5–3.8 wt% TiO_2 (Tables 1 and 2). The Ca contents were near limits of detection by AEM and microprobe analyses (CaO = <0.01–0.1 wt%). Biotite from metamorphic rocks of the amphibolite facies usually contains such TiO_2 and CaO contents (e.g., Kwak, 1968; Dymek, 1983). Most biotite analyses in the present study have interlayer-cation deficiencies (0.07–0.25 vacancies per 22 O), as is common in biotite (Foster, 1960a, 1960b). Numbers of cations for structural formulae of the sagenitic biotite were plotted according to the several schemes (not shown) that have been suggested by Dymek (1983). The results imply that substitution of Ti for octahedral cations is accompanied principally by vacancies in octahedral sites or substitution of O for OH with subordinate Ti-Tschermak's substitution. There is also a clear positive trend of Fe/(Fe + Mg) ratios with Ti contents (Fig. 9). This relationship has been considered to be controlled by crystal-chemical factors (as the biotite coexists with Ti-rich phases ilmenite or rutile) that concern the misfit between tetrahedral and octahedral sheets in phyllosilicates (Dallmeyer, 1974; Guidotti et al., 1975, 1977). Generally, substitution of larger Fe^{2+} ions for Mg^{2+} compensates for the misfit resulting from the substitution of smaller Ti^{4+} ions in octahedral sheets of biotite and thus enhances Ti substitution. A positive correlation between Fe/(Fe + Mg) and $^{[4]}Al$ in chlorite and corrensite, controlled by similar crystal-chemical factors, was discussed by Shau et al. (1990).

The Ti content of synthetic phlogopite increases with increasing temperature, as was demonstrated in hydrothermal experiments by Robert (1976) and Tronnes et al. (1985). Their experimental results are consistent with most analyses of natural biotite from igneous and metamorphic rocks. For example, biotite in igneous rocks often contains more Ti than biotite in metamorphic rocks (Rimšaite, 1964; Velde, 1969), and the Ti content of biotite coexisting with Ti-rich minerals such as ilmenite, rutile, or titanite generally increases with metamorphic grade (e.g., Kwak, 1968; Guidotti et al., 1977; Dymek, 1983). Igneous biotite usually has more Ca than metamorphic biotite, and Ca is assumed to occupy interlayer sites (cf. Deer et al., 1962a; Rimšaite, 1964; Guidotti, 1984; Speer, 1984). Olesch (1979) showed that the extent of clintonite $[Ca_2(Mg_4Al_2)Si_2Al_6O_{20}(OH)_4]$ solid solution in phlogopite $[K_2Mg_6Si_6Al_2O_{20}(OH)_4]$ increases with temperature from 13 mol% at 800 °C to 20 mol% at 1020 °C. In summary, the extent of solid solution for both Ti and Ca in biotite generally increases with increasing temperature.

Origin of the sagenitic inclusions

Because the origin of the rutile and titanite inclusions is related to and requires an understanding of the geological history of Tananao complex, a brief description is given here. A detailed description of the geological history of the Tananao complex was given by Ho (1988). Beginning in late Paleozoic time, approximately 50000 m of pre-Tertiary sediments, primarily clays and carbonates, were deposited on the continental shelf. Fragments of oceanic crust were emplaced and intermittent volcanism produced basaltic flows and pyroclastic rocks several times during sedimentation. Cretaceous, biotite-bearing granites subsequently intruded the resulting thick pile of sedimentary and volcanic rocks. The entire sequence was deformed and metamorphosed in at least three episodes, with peak metamorphism of the first two occurring at conditions up to amphibolite facies (T = 600 and 700 ± 50 °C, respectively, P = 5 kbar) and the final one under

conditions of the greenschist facies (T = 350–475 °C and P = 5 kbar) (Chen et al., 1983). The orthogneiss was derived from the granitic intrusions following the second amphibolite facies metamorphism. The entire sequence of metamorphic rocks, consisting of schists, amphibolites, serpentinites, marbles, metabasites, and gneisses, was known as the Tananao schists in the past but as the Tananao complex in recent years.

Yang and Wang Lee (1981) found that titanite is a common accessory mineral in the gneisses and other metamorphic rocks of the Tananao complex and that titanite has wholly or partially replaced ilmenite in the orthogneisses and amphibolites derived from basic igneous rocks. They thus concluded that titanite was stable and should have crystallized if Ti, Ca, and Si were available under the metamorphic conditions for the Tananao complex. Rutile was also shown to be stable in the temperature and pressure ranges of the metamorphism (cf. Jamieson and Olinger, 1969).

Preferred orientation occurring in two intimately coexisting phases is commonly a result of exsolution or topotaxial (topotactic) or epitaxial intergrowth. However, exsolution requires that the reactant components are equal to those of the sum of the products; simple exsolution of titanite and rutile is therefore precluded, as the addition of rutile and titanite components to the biotite leads to a nonsensible formula for the hypothetical precursor. The process must therefore involve addition or loss of one or more components. Because Ti and Ca are common components of biotite and because rutile and titanite are randomly distributed throughout biotite, the source of the Ti and Ca of titanite and rutile was most likely as a solid solution component of the biotite. These relations collectively require dissolution and recrystallization of at least a portion of the original biotite, with gain or loss of components.

As discussed above, the solubilities of Ti and Ca in biotite generally increase with increasing temperature. If biotite of an igneous origin was metamorphosed under the amphibolite or greenschist facies conditions determined for the Tananao complex, high Ti and Ca components inherited from higher temperature conditions could well be in excess of the limits allowed at lower temperatures. Reactions involving the breakdown of the Ti- and Ca-rich biotite to Ti- and Ca-depleted biotite plus titanite, rutile, and other phases might thus take place during metamorphism when biotite with high Ti and Ca contents was no longer stable. Studies of hydrothermal experiments also showed that Ti-rich phlogopite forming at higher temperatures ($\gtrsim$1000 °C) breaks down to assemblages of Ti-depleted phlogopite, rutile, and sanidine or vapor at lower temperatures ($\lesssim$800 °C) (Forbes and Flower, 1974; Tronnes et al., 1985). They also showed that the Ti content of phlogopite increases with increasing temperature and decreasing pressure for a given bulk TiO_2 content.

Alternatively, titanite and rutile could have formed concomitantly with the topotaxial breakdown of biotite to chlorite (cf. Veblen and Ferry, 1983; Eggleton and Banfield, 1985) during an early retrogressive episode of polymetamorphism. Titanite or rutile formed in this manner would likely be observed as well-oriented acicular inclusions in chlorite, as reported by Rimšaite (1964), although titanite usually occurs as relatively large crystals without preferred orientation in chlorite (Dodge, 1973; Ferry, 1979; Parry and Downey, 1982; Veblen and Ferry, 1983). Baxter and Peacor (unpublished data) observed both titanite and rutile intergrown with interlayered chlorite and biotite in samples of altered tuffaceous rocks from New Zealand, where the chlorite was an alteration product of Ti-rich detrital biotite. Ferry (1979) suggested a reaction that accounts for the formation of chlorite and titanite from Ti-bearing biotite by hydrothermal alteration in granitic rocks. The chlorite thus formed in an early stage of retrograde metamorphism might have transformed topotaxially to biotite and retained well-oriented titanite and rutile in biotite during a final progressive episode of the polymetamorphism, which occurred at the conditions well above the biotite isograd according to several prograde reactions (e.g., Ernst, 1963; Brown, 1971).

However, since a sagenitic biotite with well-oriented inclusions of titanite and rutile may also be altered to chlorite and retain the preexisting inclusions in chlorite, existence of sagenitic chlorite does not necessarily imply that the titanite and rutile inclusions formed during alteration of biotite to chlorite. In addition, titanite, which has been characterized as one of the products during alteration of biotite to chlorite, does not generally occur as well-oriented, needlelike inclusions like those in this study (Dodge, 1973; Ferry, 1979; Parry and Downey, 1982; Veblen and Ferry, 1983). Therefore, it is more likely that the sagenitic biotite formed by a precipitation mechanism where titanite, rutile, and Ti-depleted biotite crystallized topotaxially during metamorphism through the breakdown of a Ti- (and Ca-) rich biotite that had formed under conditions of higher temperatures (e.g., igneous biotite) than those of the metamorphism.

Chlorite observed in the present investigation, which is presumed to replace biotite or overgrow biotite during the latest greenschist facies metamorphism, does not contain well-oriented acicular inclusions. It apparently has no relationship with the formation of acicular inclusions in biotite. In addition, the rutile inclusions in biotite contain precipitated hematite-ilmenite platelets that should postdate the formation of rutile (cf. Banfield and Veblen, 1991). Precipitation of hematite in rutile took place within an approximate temperature range of 450–600 °C, according to observations of experimentally annealed rutile (Putnis, 1978; Putnis and Wilson, 1978), though the precipitation temperatures are probably lower, based on the observations by Banfield and Veblen (1991) and Bursill et al. (1984). Therefore, precipitation of rutile and titanite in the sagenitic biotite probably took place during the amphibolite facies metamorphism or following retrograde metamorphism at temperatures higher than those of the latest greenschist facies metamorphism for the Tananao complex. Other examples of precipitated inclusions, such

as well-oriented magnetite inclusions in pyroxenes (Fleet et al., 1980) and hematite inclusions in sillimanite (Fleet and Arima, 1985), have been reported as occurring in metamorphic rocks with a complex retrograde history.

Structural control of the well-oriented inclusions in biotite

Optical and TEM observations showed that one of the three sets of intersecting rutile needles forming asterisks is parallel to **b** of biotite. The prism axes of rutile needle are parallel to **c**, and (100) or (010) of rutile are parallel to (001) of biotite. The rutile structure is composed of parallel chains of edge-sharing TiO_6 octahedra that extend parallel to **c** and are connected laterally by sharing vertices. The O layer, which is parallel to (100) or (010) of rutile, is nearly closest-packed, though slightly puckered. The biotite structure is also based on closest packing of anions, with anion layers being parallel to (001) of biotite. (Drawings of the rutile and biotite structures can be found in many standard textbooks of mineralogy and will not be given here.) Preferred orientation involving (100) or (010) of rutile and (001) of biotite is therefore understandable in terms of their similar closest-packed geometries. Furthermore, the $(Mg,Fe,Al,Ti)(O,OH)_6$ octahedra of the brucite-like octahedral sheet of biotite form chains of octahedra by sharing edges, as in rutile. Such chains extend in three directions, each oriented 60° from the others and conforming to the pseudohexagonal symmetry of (001) of biotite. During dissolution (of biotite) and crystallization (of rutile), migration of Ti into those octahedra in substitution of Mg, Al, and Fe and replacement of OH by O could easily convert the edge-sharing $(Mg,Fe,Al,Ti)(O,OH)_6$ octahedra into chains of edge-sharing TiO_6 octahedra to form a pattern of three rutile needles with ends intersecting at angles of 120° (Fig. 4). Superposition of another pattern that consists of three needles extending in the directions opposite to those of the first pattern creates an asterisk pattern with adjacent needles at angles of 60° (Figs. 1 and 4). Growth of rutile needles thus involves minimum reconstruction and cation diffusion.

Fleet and Arima (1985) studied oriented hematite inclusions in sillimanite and indicated that ⟨120⟩ of hematite is parallel to **c** of sillimanite, which is the direction containing chains of edge-sharing octahedra for both phases. The orientation relationships of magnetite inclusions in pyroxenes, including $\{111\}_M \| \{100\}_P$ and $\langle 112\rangle_M \| \mathbf{c}_P$, are also related to closest-packed O layers and chains of edge-sharing octahedra (Fleet et al., 1980). Platelets of hematite or $(Fe,Ti)_2O_3$ inclusions in rutile with $\{001\}_H \| \{100\}_R$ and $\langle 120\rangle_H \| \mathbf{c}_R$ have been observed in the present and other studies (Putnis and Wilson, 1978; Putnis, 1978; Bursill et al., 1984; Banfield and Veblen, 1991). Gilkes and Suddhiprakarn (1979) reported a preferred orientation between goethite and biotite with $\{100\}_G \| \{001\}_B$ and $\mathbf{c}_G \| \mathbf{b}_B$ in deeply weathered granitic rocks, although other orientations between goethite and biotite have been observed by Banfield and Eggleton (1988). All these preferred crystallographic relations between rutile and biotite, magnetite and pyroxenes, rutile and hematite, and goethite and biotite have a common structural similarity, in that the two coexisting phases share nearly closest-packed anion layers and chains of edge-sharing octahedra within the anion layers and are thus topotaxially controlled (cf. Fleet, 1982; Fleet and Arima, 1985).

Although most titanite inclusions exhibit preferred orientation in biotite, TEM data have shown that many different orientations with respect to (001) of biotite also occur. It is estimated that more than 80% of the titanite inclusions are elongated parallel to ⟨011⟩ and to the three directions forming equilateral triangles, with $\{11\bar{1}\}$ or $\{43\bar{3}\}$ of titanite approximately parallel to {001} of biotite. However, in contrast to the single kind of orientation occurring almost exclusively for rutile, other orientations in which {001}, $\{10\bar{1}\}$, $\{01\bar{1}\}$, or $\{\bar{4}10\}$ of titanite are parallel to {001} of biotite were also observed. An orientation with {110} of titanite parallel to {001} of mixed-layer biotite-chlorite in altered granitic biotite from southeastern Australia was observed by Eggleton and Banfield (1985). The variable orientations of titanite with respect to {001} of biotite indicate that titanite does not have well-defined structural features in common with biotite. Nevertheless, the preferred orientation $\langle 011\rangle_T \| \mathbf{a}_B$ implies some structural control, but we have been unable to define one.

Acknowledgments

The authors are grateful to Eric J. Essene, Tamsin C. McCormick, and J. Alexander Speer for critical reviews of the manuscript. We thank Pouyan Shen and Su-Cheng Yu for many helpful discussions. Transmission and analytical electron microscopic work was carried out at the Institute of Mining, Metallurgy and Material Sciences of the National Cheng Kung University and the Institute of Materials Science and Engineering of the National Sun Yat-Sen University in Taiwan, Republic of China, and in the Electron Microbeam Analysis Laboratory, the University of Michigan, Ann Arbor, Michigan. A titanite standard (B20360) for AEM analyses was kindly provided by the National Museum of Natural History, Smithsonian Institution. The present study was supported by the grants NSC-67M-0202-12(02), NSC-75-M006-0202-03, and NSC-76-M006-0202-02 to H.-Y.Y. from the National Science Council of the government of the Republic of China, and by NSF grant EAR-8817080 to D.R.P. The CM-12 STEM was acquired under NSF grant EAR-8708276 and the electron microprobe under NSF grant EAR-8212764. Contribution no. 476 from the Mineralogical Laboratory, Department of Geological Sciences, University of Michigan, Ann Arbor, Michigan 48109, U.S.A.

References cited

Banfield, J.F., and Eggleton, R.A. (1988) Transmission electron microscope study of biotite weathering. Clays and Clay Minerals, 36, 47–60.

Banfield, J.F., and Veblen, D.R. (1991) The structure and origin of Fe-bearing platelets in metamorphic rutile. American Mineralogist, 76, 113–127.

Bohlen, S.R., Peacor, D.R., and Essene, E.J. (1980) Crystal chemistry of a metamorphic biotite and its significance in water barometry. American Mineralogist, 65, 55–62.

Brown, E.H. (1971) Phase relations of biotite and stilpnomelane in the greenschist facies. Contributions to Mineralogy and Petrology, 31, 275–299.

Bursill, L.A., Blanchin, M.G., and Smith, D.J. (1984) Precipitation phenomena in non-stoichiometric oxides II. {100} platelet defects in reduced rutiles. Proceedings of the Royal Society of London, A 391, 373–391.

Chen, C.H., Chu, H.T., Liou, J.G., and Ernst, W.G. (1983) Explanatory notes for the metamorphic facies map of Taiwan. Special Publication of the Central Geological Survey, no. 2, p. 1–32. The Ministry of Economic Affairs, Taipei, Republic of China.

Cliff, G., and Lorimer, G.W. (1975) The quantitative analysis of thin specimens. Journal of Microscopy, 103, 203–207.

Dallmeyer, R.D. (1974) The role of crystal structure in controlling the partitioning of Mg and Fe^{2+} between coexisting garnet and biotite. American Mineralogist, 59, 201–203.

Deer, W.A., Howie, R.A., and Zussman, J. (1962a) Rock-forming minerals, vol. 3: Sheet silicates, 270 p. Longman, London.

——— (1962b) Rock-forming minerals, vol. 5: Non-silicates, 371 p. Longman, London.

——— (1982) Rock-forming minerals, vol. 1A: Orthosilicates (2nd edition), 919 p. Longman, London.

Dodge, F.C.W. (1973) Chlorites from granitic rocks of the central Sierra Nevada batholith, California. Mineralogical Magazine, 39, 58–64.

Dymek, R.F. (1983) Titanium, aluminum and interlayer cation substitutions in biotite from high-grade gneisses, West Greenland. American Mineralogist, 68, 880–899.

Eggleton, R.A., and Banfield, J.F. (1985) The alteration of granitic biotite to chlorite. American Mineralogist, 70, 902–910.

Ernst, W.G. (1963) Significance of phengitic micas from low-grade schists. American Mineralogist, 48, 1357–1373.

Ferry, J.M. (1979) Reaction mechanism, physical conditions, and mass transfer during hydrothermal alteration of mica and feldspar in granitic rocks from south-central Maine, USA. Contributions to Mineralogy and Petrology, 68, 125–139.

Fleet, M.E. (1982) Orientation of phase and domain boundaries in crystalline solids. American Mineralogist, 67, 926–936.

Fleet, M.E., and Arima, M. (1985) Oriented hematite inclusions in sillimanite. American Mineralogist, 70, 1232–1237.

Fleet, M.E., Bilcox, G.A., and Barnett, R.L. (1980) Oriented magnetite inclusions in pyroxenes from the Grenville province. Canadian Mineralogist, 18, 89–99.

Forbes, W.C., and Flower, M.F.J. (1974) Phase relations of titan-phlogopite, $K_2Mg_4TiAl_2Si_6O_{20}(OH)_4$: A refractory phase in the upper mantle? Earth and Planetary Science Letters, 22, 60–66.

Foster, M.D. (1960a) Layer charge relations in the dioctahedral and trioctahedral micas. American Mineralogist, 45, 383–398.

——— (1960b) Interpretation of the compositions of trioctahedral micas. U.S. Geological Survey Professional Paper 354-B, 11–48.

Gary, M., McAfee, R., Jr., and Wolf, C.F. (1972) Glossary of geology, 805 p. American Geological Institute, Washington, DC.

Gilkes, R.J., and Suddhiprakarn, A. (1979) Biotite alteration in deeply weathered granite. II. The oriented growth of secondary minerals. Clays and Clay Minerals, 27, 361–367.

Guidotti, C.V. (1984) Micas in metamorphic rocks. In Mineralogical Society of America Reviews in Mineralogy, 13, 357–467.

Guidotti, C.V., Cheney, J.T., and Conatore, P.D. (1975) Interrelationship between Mg/Fe ratio and octahedral Al content in biotite. American Mineralogist, 60, 849–853.

Guidotti, C.V., Cheney, J.T., and Guggenhein, S. (1977) Distribution of titanium between coexisting muscovite and biotite in pelitic schists from northwestern Maine. American Mineralogist, 62, 438–448.

Hewitt, D.A., and Wones, D.R. (1984) Experimental phase relations of the micas. In Mineralogical Society of America Reviews in Mineralogy, 13, 201–247.

Higgins, J.B., and Ribbe, P.H. (1976) The crystal chemistry and space groups of natural and synthetic titanites. American Mineralogist, 61, 878–888.

Hirsch, P.B., Howie, A., Nicholson, R.B., Pashley, D.W., and Whelan, M.J. (1977) Electron microscopy of thin crystals (2nd edition), 563 p. Kreiger, Huntington, New York.

Ho, C.S. (1988) An introduction to the geology of Taiwan. Explanatory text of the geological map of Taiwan (2nd edition), 192 p. Central Geological Survey, The Ministry of Economic Affairs, Taipei, Republic of China.

Jamieson, J.G., and Olinger, B. (1969) Pressure-temperature studies of anatase, brookite, rutile, and TiO_2 (II): A discussion. American Mineralogist, 54, 1477–1481.

Kwak, T.A.P. (1968) Ti in biotite and muscovite as an indication of metamorphic grade in almandine amphibolite facies rocks from Sudbury, Ontario. Geochimica et Cosmochimica Acta, 32, 1222–1229.

Lo, C.H., and Wang Lee, C.M. (1981) Mineral chemistry in some gneissic bodies, the Hoping-Chipan area, Hualien, eastern Taiwan. Proceedings of the Geological Society of China, 24, 40–55.

Miser, D.E., and Buseck, P.R. (1988) Defect microstructures in oxygen-deficient rutile from Fe^0-bearing xenoliths from Disko, Greenland. Geological Society of America Abstracts with Program, 20, A101.

Moorhouse, W.W. (1959). The study of rocks in thin sections, 514 p. Harper and Row, New York.

Niggli, Von C.R. (1965) Über die Natur sagenitartig angeordneter Nadeln in Biotit. Schweizer Mineralogische und Petrographische Mitteilungen, 45, 807–817.

Olesch, M. (1979) Ca-bearing phlogopite: Synthesis and solid solubility at high temperatures and pressures of 5 and 10 kilobars. Bulletin de Minéralogie, 102, 14–20.

Parry, W.T., and Downey, L.M. (1982) Geochemistry of hydrothermal chlorite replacing igneous biotite. Clays and Clay Minerals, 30, 81–90.

Putnis, A. (1978) The mechanism of exsolution of hematite from natural iron-bearing rutiles. Physics and Chemistry of Minerals, 3, 183–197.

Putnis, A., and Wilson, M.M. (1978) A study of iron-bearing rutiles in the paragenesis TiO_2-Al_2O_3-P_2O_5-SiO_2. Mineralogical Magazine, 42, 255–263.

Rimšaite, J. (1964) On micas from magmatic and metamorphic rocks. Beitrage zur Mineralogie und Petrographie, 10, 152–183.

Rimšaite, J., and Lachance, G.R. (1966) Illustrations of heterogeneity in phlogopite, feldspar, euxenite and associated minerals. Fourth General Meeting, International Mineralogical Association, Mineralogical Society of India IMA Volume, 209–229.

Robert, J.-L. (1976) Titanium solubility in synthetic phlogopite solid solution. Chemical Geology, 17, 213–227.

Rumble, D. (1976) Oxide minerals in metamorphic rocks. In Mineralogical Society of America Reviews in Mineralogy, 3, R-1–24.

Shau, Y.-H., Peacor, D.R., and Essene, E.J. (1990) Corrensite and mixed-layer chlorite/corrensite in metabasalt from northern Taiwan: TEM/AEM, EMPA, XRD, and optical studies. Contributions to Mineralogy and Petrology, 105, 123–142.

Shau, Y.-H., Feather, M.E., Essene, E.J., and Peacor, D.R. (1991) Genesis and solvus relations of submicroscopically intergrown paragonite and phengite in a blueschist from northern California. Contributions to Mineralogy and Petrology, 106, 367–378.

Speer, J.A. (1984) Micas in igneous rocks. In Mineralogical Society of America Reviews in Mineralogy, 13, 299–349.

Speer, J.A., and Gibbs, G.V. (1976) The crystal structure of synthetic titanite, $CaTiOSiO_4$, and the domain textures of natural titanites. American Mineralogist, 61, 238–247.

Taylor, M., and Brown, G.E. (1976) High-temperature structural study of the $P2_1/a = A2/a$ phase transition in synthetic titanite, $CaTiSiO_5$. American Mineralogist, 61, 435–447.

Tronnes, R.G., Edgar, A.D., and Arima, M. (1985) A high pressure-high temperature study of TiO_2 solubility in Mg-rich phlogopite: Implications to phlogopite chemistry. Geochimica et Cosmochimica Acta, 49, 2323–2329.

Veblen, D.R., and Ferry, J.M. (1983) A TEM study of the biotite-chlorite reaction and comparison with petrologic observation. American Mineralogist, 68, 1160–1168.

Velde, D. (1969) Les micas des lamprophyres: Kersantites, minettes et lamproites. Bulletin de la Société Francaise de Minéralogie et de Cristallographie, 92, 203–223.

Winchell, A.N. (1961) Elements of optical mineralogy. Part II. Description of minerals (4th edition), 283 p. Wiley, New York.

Yang, H.Y., and Wang Lee, C.M. (1981) Fe-Ti oxide minerals in some Tananao schists and their bearing on metamorphism. Memoir of the Geological Society of China, 4, 537–550.

Manuscript received April 23, 1990
Manuscript accepted April 17, 1991